1   *Article*

2 Key Parameters in the Manufacture of SiC-Based
3 Composite Materials by Reactive Melt Infiltration

4   **Mario Caccia [1,2], Javier Narciso [1,3,*]**

5   [1] Institute of Materials (IUMA), Alicante University, Alicante, Spain
6   [2] Materials Engineering Department, Purdue University, West Lafayette, USA
7   [3] Department of Inorganic Chemistry, Alicante University, Alicante, Spain
8   [4] Center for Materials Science and Nanotechnology, Department of Chemistry, University of Oslo, Oslo,
9   Norway
10 *   Correspondence: narciso@ua.es;

11 **Abstract:** The manufacture of SiC-based composites is quite widespread, and currently different
12 methods are employed for to produce them. The most efficient method, taking into account the
13 cost/performance ratio, is reactive melt infiltration. It consists in infiltrating liquid silicon into a
14 porous preform that must contain carbon, so that SiC is produced during infiltration. This chemical
15 reaction is, in fact, the driving force of the process. In the present work, the synthesis of two SiC-
16 based composite materials with very different applications and microstructures has been studied
17 and optimized. In both cases, materials have been obtained with suitable properties for the selected
18 applications. One of the materials studied is SiCp/Si for protection systems such as armor jackets,
19 and the other one is C_f/SiC for use in braking systems. For the optimization, the dwell time and the
20 atmosphere (Ar or primary vacuum) were used as variables. It has been found that in both preforms
21 the optimum conditions are 1 hour dwell time and a vacuum atmosphere at 1450 °C. The effect of
22 these parameters on microstructure and infiltration kinetics are discussed.

23 **Keywords:** SiC; CMCs ; reactive infiltration
24

25 1. Introduction

26 Composite materials with a high volume fraction of SiC possess attractive properties for high-

27 temperature applications (e.g. high stiffness, excellent corrosion and abrasion/erosion resistance, low

28 thermal expansion coefficient and low density). This kind of composites, SiC_P/Si in particular have

29 also shown an excellent behavior as armor systems, being able to absorb large amounts of energy

30 upon an impact [1-4]. Their low density and their effectiveness as armor materials make them ideal

31 candidates for ground transportation and personal armor devices. Nowadays armor jackets are

32 already being manufactured containing SiC_P/Si composites. The most common arrangements of

33 CMCs within bullet-proof jackets is in hexagons or squares. Furthermore, given the low coefficients

34 of thermal expansion of SiC_P/Si composites, they are excellent candidates for primary shields in future

35 reusable spacecraft where they could protect against micrometeorites and other space particles

36 impact, been also able to withstand the atmosphere reentry process [5]. These kinds of composites

37 can be easily manufactured with the reactive melt infiltration technique, which provides the

38 possibility of synthesizing a great variety of geometries [6-12] due to its shape preservation

39 capabilities.

40   On the other hand C_f/SiC composite materials, manufacture by reactive infiltration, have replaced
41   conventional carbon steel brake discs in extreme applications such as airplanes and racing cars
42   because of their superior performance, they lower density, and their higher wear resistance. These
43   kind of composite materials have been tested by NASA under atmosphere re-entry conditions as well
44   because of their potential use in space pods and future reusable space transportation systems (STS)
45   [5]. They exhibit higher specific stiffness than some metal alloys and improved corrosion resistance
46   compared to carbon/carbon composite materials. Furthermore, if coatings are applied, the corrosion
47   by oxidation during re-entry to earth's atmosphere can be substantially reduced.

48   The main objective of this work is to identify and optimize the most relevant experimental
49   parameters, namely, dwell time and atmosphere, and to determine how these parameters affect the
50   microstructure and the mechanical properties of such composite materials. For a better
51   understanding of the infiltration process, an exhaustive characterization of the porous preform was
52   made. Given their different chemical composition, the process limiting infiltration kinetics differs
53   thus affecting the optimization of the main infiltration parameters.

54

55   **2. Materials and Methods**

56   2.1 Preform characterization

57   The porous preforms used in this work were supplied by different companies member of the 7th
58   Framework European project *High-Frequency Electromagnetic Technologies for Processing of Advanced*
59   *materials and Graphite Expansion* (H.E.L.M project) [13] and present diverse microstructures and pore
60   systems. Their chemical composition was studied using X ray diffraction (XRD) and
61   thermogravimetric analysis (TGA), their density and porosity were determined by combining water
62   and He picnometry (Acupyc 1330TC, Micrometrics), and their pore size distribution was obtained
63   using Hg porosimetry (Poremaster-60, Quantachrome Instruments). The microstructure was studied
64   using various microscopy techniques. A detailed description of the experimental techniques can be
65   found in the previous works of our research groups [12-14].

66

67   SiC$_P$/C Preforms

68   SiC$_P$/C preforms were kindly supplied by Petroceramics, and they are comprised of a bimodal
69   mixture of α-SiC particles (280 and 1000 F.E.P.A grain size which is equivalent to 36.5 and 4.5 μm
70   respectively) bonded by a carbon matrix. These preforms were made by mechanically mixing α-SiC
71   (black SiC, 99.5% purity) with 10 wt.% phenolic resin (Bakelite, Germany). The mixture was
72   uniaxially pressed at 140 MPa and 150 °C to promote cross-linking of the resin. After that, the pressed
73   mixture was pyrolyzed under a nitrogen atmosphere at 700 °C. Samples were supplied in the shape
74   of bars with dimensions of 50x8x4 mm^3.

75

76   C_f/C Preforms

77   C_f/C preforms were kindly supplied by BremboSGL group and are comprised of a mixture of
78   chopped PAN-derived carbon fibers embedded in a carbon matrix. This preform was made by
79   pressing a dry mixture of carbon fibers and phenolic resin (Bakelite, Germany) at 150 ℃ to promote
80   cross-linking of the resin. Finally, pyrolysis of the product at 900 ℃ was performed to obtain a C_f/C
81   porous composite.
82
83   2.2 Reactive infiltration and infiltration kinetics
84
85   Infiltration experiments were performed both, under Ar flow and under vacuum, following the
86   procedure described in a previous paper [14-16]. Because the experiments are performed using
87   resistance furnaces, the heating rates that can be achieved (< 8 ℃/min) do not allow to accurately
88   study the effect of temperature on infiltration. Since infiltration starts and proceeds rapidly after
89   melting of Si (1410 ℃), it is impossible to achieve isothermal conditions at higher temperatures
90   without having some previous infiltration. For this reason, experimental temperature was fixed to
91   1450 ℃, slightly above the melting point of Si to ensure complete melting.
92   Because of the differences between SiC/C and C_f/C preforms, different behaviors during infiltration
93   are expected. Since molten Si wets SiC, infiltration in the SiC/C preform should not be limited by the
94   chemical reaction between C and Si, and should proceed immediately after carbon dissolution. The
95   laws of fluid dynamics will thus govern infiltration kinetics. Since the content in C in this preform is
96   rather low, and is only intended to provide a good bonding between the reinforcement and the
97   matrix, porosity and pore diameter should not change drastically during infiltration. On the other
98   hand, in the C_f/C preform, the content in reactive carbon is very high compared to the SiC/C preform.
99   Because molten Si does not wet carbon or carbon fibers, it is expected that in this preform, infiltration
100 will be controlled by the chemical reaction at the infiltration front, and limited by the reaction kinetics.
101 It should occur, therefore, much slower than for the SiC/C preform. In this case, where reactivity is
102 much higher, pore diameter reduction might play a major role in the infiltration kinetics.
103
104 2.3 Microstructure characterization
105 The bulk density of the composites was measured using the Archimedes method. The solid density
106 was determined using He picnometry (Acupyc 1330TC, Micrometrics). Residual porosity was
107 calculated based on density measurements as the relative difference between the solid and bulk
108 densities. The microstructure of the obtained composites was studied using optical microscopy (PM3,
109 Olympus), scanning electron microscopy (S3000N, Hitachi) and X ray diffraction (D8-advanced,
110 Bruker). Prior to microscopy characterization, cross sections of the specimes were obtained, mounted
111 in resin and polished up to a 1 μm surface finish using standard metallographic procedures. For XRD
112 the specimens were ground to powder using a ball mill with WC as milling media.
113 In the case of SiCp/Si composites, where the diffraction peaks of the β SiC phase are coincident with
114 some diffraction peaks of the α SiC phase, XRD does not allow to characterize the reaction product.

115   To overcome this issue, quantitative XRD was performed. In order to quantify the β-SiC formed

116   during infiltration, a calibration curve was first obtained using α-SiC, β-SiC and Si powder mixtures

117   with known compositions. The area ratio between the most intense common diffraction peak for both

118   phases (diffraction peak for the 111 crystalline plane at 35.65°) and the second most intense peak of

119   the α SiC phase which is not common with the β SiC phase (diffraction peak of the 103 crystalline

120   plane at 38.2°) was calculated and plotted against the molar ratio between α-SiC and β-SiC ($X_{\alpha SiC}/X_{\beta SiC}$)

121   to obtain the calibration curve. This calibration curve was then used to estimate the $X_{\alpha SiC}/X_{\beta SiC}$ in the

122   specimens.

123   To obtain the phase quantification of C_f/SiC composites, a selective etching of each phase was

124   performed with successive weight measurements. To remove the carbon fibers and the amorphous

125   carbon the samples were heat treated at 800 ℃ in air during 9 hours. To remove silicon, the remaining

126   sample was treated with concentrated hydrofluoric acid (HF 40%) at 80 ℃ during 12 hours. SiC was

127   obtained as the difference between the original weight and what remained.

128

129   2.4 Mechanical characterization

130   The mechanical properties most relevant to the potential applications were measured for each

131   composite. For the SiCp/Si composites, bending and compressive strengths were measured in a

132   Universal Testing Machine (model 4411, Instron) with the 3-point bending test and the quasi-static

133   compression test configurations following the UNE-EN-843-1:2006 standard. The 3 point bending test

134   was performed at a cross-head displacement of 0.1 mm/min (10^{-3} s^{-1}) and the compression test was

135   carried out at a strain rate of 10^{-3} s^{-1}. An extensometer was used during the bending test, and the

136   flexural modulus was calculated from these results. For C_f/SiC composites, the bending strength was

137   measure following the same procedure described for the SiC_P/Si specimens. The wear behavior of

138   this material was studied using the ball-on-disc setup (CSEM Instruments built according to ASTM

139   G99 standard). The wear test was performed at a linear speed of 10 cm/s with a load of 5 N and a

140   duration of 10 km. The average friction coefficient was measured from this test. The average Vickers

141   microhardness was also measured using a microindentor (Micromet 2100, Buehler) according to the

142   ASTM C1327 standard. Vickers microhardness was measured using a load of 1 kg with a holding

143   time of 15 s.

144

145   **3. Results and discussion**

146   3.1 Preform characterization

147   Table 1 summarizes the results of the characterization of the SiCp/C preform.

148

149   **Table 1.** Results of the characterization of the SiC_P/C preform.

Composition (wt.%)	Bulk density (g/cm³)	He density (g/cm³)	P (%)	D_{50}^* (μm)

| α-SiC	C				
95.30	4.70	2.10 - 2.20	3.10	30	1.30

150   *D_{50}: Average pore diameter measured by Hg porosimetry

151

152   The composition was obtained by TGA in oxidizing atmosphere ($N_2:O_2 = 4:1$) in the range 25-800 ºC

153   and it is 95.3 wt.% SiC and 4.7 wt.% C. The corresponding thermogram is shown in Figure 1a where

154   the first initial mass loss corresponds to moisture in the sample, and the mass loss at 600 ºC

155   corresponds to the combustion of the C phase. The remaining mass corresponds to SiC, which

156   remains unaltered in this range of temperature. XRD tests indicated that α-SiC is the only crystalline

157   phase present in the preform (see Figure 1b), exhibiting a mixture of the 4H and 6H polytypes.

158   The bulk density of the preform ranges from 2.10-2.20 g/cm³, while the He density is 3.10 g/cm³.

159   Considering these values open porosity was calculated yielding a value of around 30%.

160

161
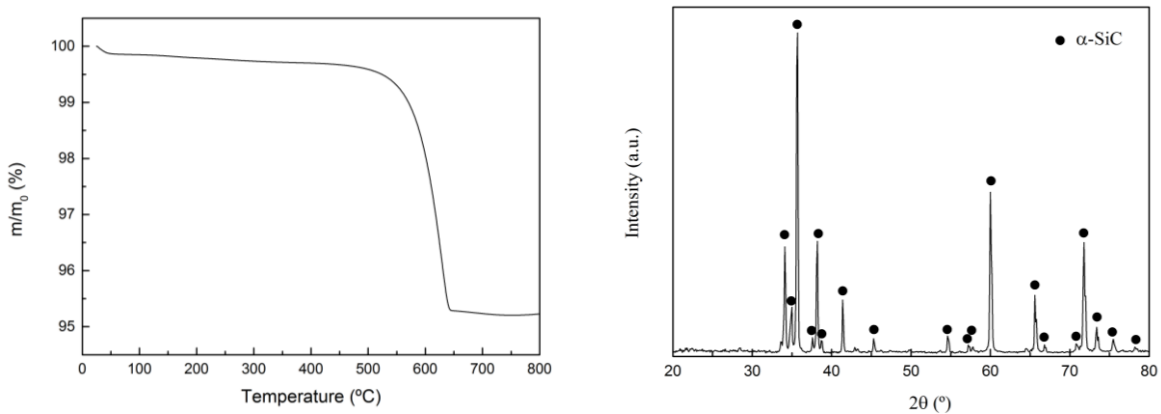
162   **Figure 1.** (a) Thermogram of the SiC/C preform in oxidizing atmosphere ($N_2:O_2 = 4:1$), (b) XRD pattern

163   for the SiC_P/C preform.

164

165   Figure 2a shows an optical microscope image of a polished cross-section of the preform, where the

166   α-SiC phase is depicted in white, the C phase in grey and the porosity in black. A homogeneous

167   distribution of the phases and the porosity is clearly observed.

168

169
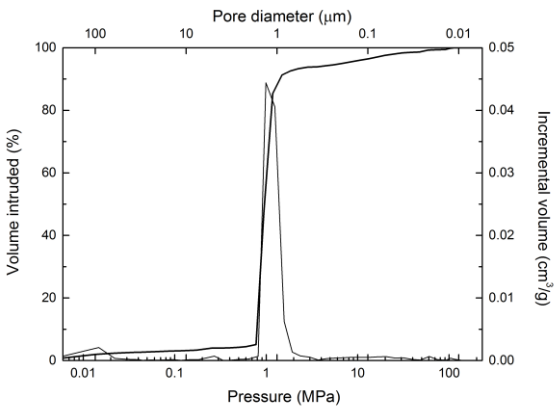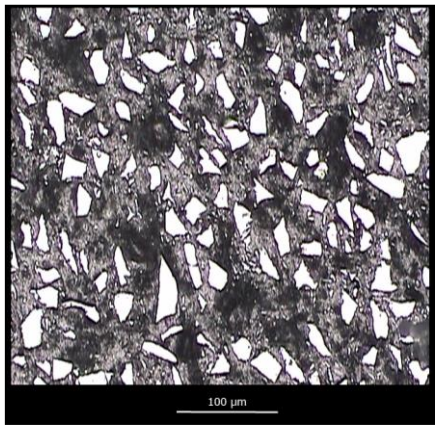
170   **Figure 2.** (a) Optical microscopy image of a polished cross-section of the SiC_P/C preform, (b) Mercury

171   intrusion curve as a function of pressure and pore size distribution for the SiC_P/C preform.

172

173   Mercury porosimetry showed a narrow pore size distribution around a pore size of 1 micron (P = 1

174   MPa). The intrusion curve and the pore size distribution derived from it are shown in Figure 2b.

175   Table 2 summarizes the results of the characterization of the preform.

176

177   **Table 2.** Results of the characterization of the C_f/C preform.

Composition (wt.%)		Bulk density (g/cm³)	He density (g/cm³)	P (%)	D_{50} (μm)
C_f	C				
70	30	1.20 -1.25	1.83	30	13.40

178

179   The composition was obtained by TGA in oxidizing atmosphere (N_2:O_2 = 4:1) in the range 25-900 °C

180   and it is 70 wt.% carbon fiber and 30 wt.% carbon binder. The corresponding thermogram is shown

181   in Figure 3a where the first initial mass loss corresponds to moisture in the sample, and the mass loss

182   at 600 °C corresponds to the combustion of the amorphous C binder (product of pyrolysis of the

183   phenolic resin). The final mass loss observed at 750 °C corresponds to the combustion of the PAN-

184   derived carbon fibers, which are thermally more stable than the amorphous C binder. XRD tests

185   indicated that carbon fibers are the only crystalline phase (See Figure 3b). However they present low

186   crystallinity (very broad diffraction peak) as the spacing between graphitic layers calculated from the

187   position of the 0002 peak (0.35 nm) is far from the theoretical one for perfect graphite (0.33 nm).

188

189
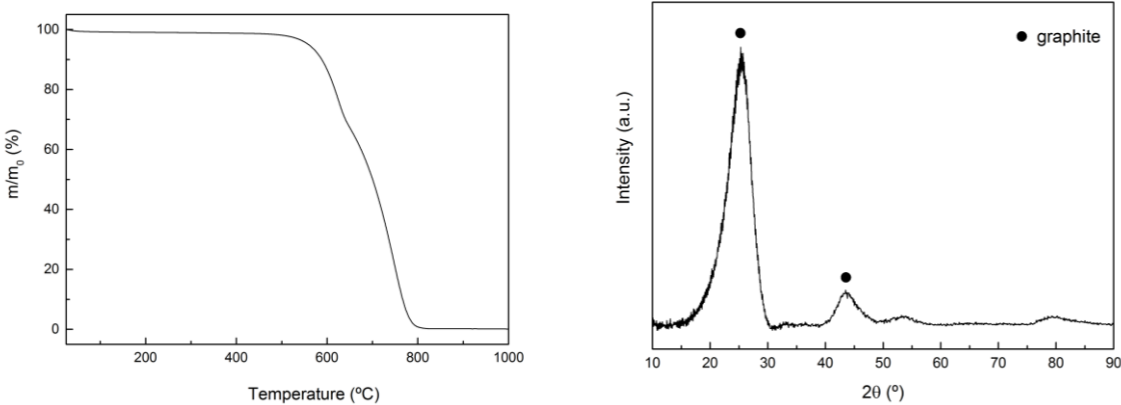
190   **Figure 3.** (a)Thermogram of the C_f/C preform in oxidizing atmosphere (N_2:O_2 = 4:1), (b) XRD pattern

191   for the C_f/C preform.

192

193   The bulk density of the preform ranges from 1.20-1.25 g/cm³, while the He density is 1.83 g/cm³.

194   Considering these values open porosity was calculated yielding a value of around 30%.

195   Figure 4a shows an optical microscope image of a polished cross-section of the preform, where the
196   cross section of the carbon fibers is easily distinguished as they appear in the shape of circles or
197   ellipses depending on the direction of the fiber. By looking at the microstructure, it becomes clear
198   that fibers are randomly oriented and grouped in fiber bundles. The carbon binder is observed
199   surrounding the fibers and fiber bundles, and porosity of different sizes is distinguished.
200
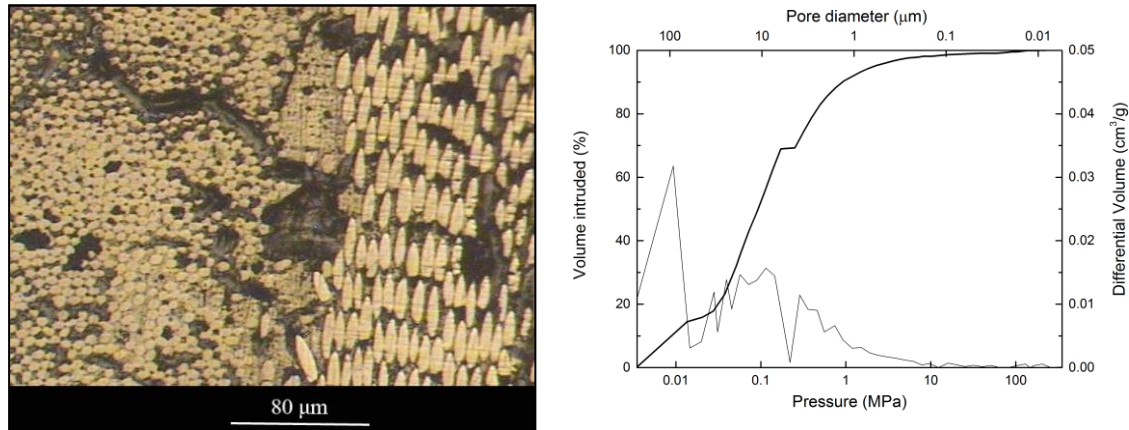
201
202   **Figure 4.** (a) Optical microscopy image of a polished cross-section of the C_f/C preform, (b) Mercury
203   intrusion curve as a function of pressure and pore size distribution for the C_f/C preform.
204

205   Figure 4b shows the intrusion curve and the pore size distribution obtained from mercury
206   porosimetry. Figure 8 shows a broad distribution of pore sizes around two values, 2 and 10 μm. This
207   is in agreement with the porosity observed in Figure 6. The pores with sizes around 2 μm correspond
208   to the interfiber spaces, while the pores with sizes around 10 μm correspond to the interbundle
209   spaces. The high initial intrusion can be attributed to the filling between the pieces of sample rather
210   than to actual porosity of the material.
211

212   3.2 Infiltration of SiC_P/C and C_f/C porous preforms
213

214   The time required for full infiltration of a typical 5 mm thick preform was calculated for both
215   preforms using Darcy's equation :

216    $$h^2 = \frac{2 \cdot K \cdot t}{\eta \cdot \Phi} \cdot \Delta P$$

217   Where h is the infiltrated distance, K the permeability, t time, η the fluid dynamic viscosity, Φ the
218   porosity of the system and ΔP the pressure drop that drives the infiltration. The permeability is
219   proportional to the pore radius according to:

220    $$K = a \cdot r^2$$

221   Where a is a proportionality constant and r the average pore radius. In the case of systems where
222   the liquid wets the solid and infiltration proceeds spontaneously (θ < 90°), the pressure drop is the
223   capillary pressure (P_c) given by:

224
$$P_c = \frac{2 \cdot \lambda \cdot \gamma_{LV} \cdot cos\theta \cdot (1 - \Phi)}{r \cdot \Phi}$$

225 Where λ is a geometrical factor, γ_{LV} the surface tension of the liquid, θ the contact angle of the liquid
226 on the solid, Φ the porosity of the system, and r the average pore radius. Table 3 shows the
227 parameters for the Si-C systems used to calculate the infiltration time.

228

229 **Table 3.** *Parameters used for the calculation of the infiltration time of liquid Si on the different preforms at*
230 *1450 °C.*

Symbol	Magnitude	Value	SI units	Reference
λ	Geometrical factor	2-4	-	[17-19]
a	Proportionality constant	$4 \cdot 10^{-4}$	-	[8]
γ_{LV}	Surface tension	0.750	N/m	[20-22]
θ	Contact angle of Si on C	40	°	[23]
η	Dynamic viscosity of liquid Si	$0.605 \cdot 10^{-3}$	Pa·s	[20]

231

232 This model suggests that vertical infiltration of a preform of 5 mm thickness should be achieved
233 within a fraction of seconds, 0.54 s for the SiC/C preform and 0.05 s for the C_f/C preform. However,
234 it must be considered that the time required for full infiltration of a 3D sample is higher, since the
235 melt has to spread in the x and z directions, and usually permeability in this directions is a couple of
236 orders of magnitude lower for uniaxially pressed materials [24]. Nevertheless, these models are likely
237 to predict a time for full infiltration of a couple of orders of magnitude faster than the real one, since
238 infiltration in the C_f/C preform should be limited by the chemical reaction at the infiltration front.
239 Furthermore, none of these models take into account the pore reduction or closure phenomena which
240 might play a major role in infiltration kinetics. The infiltration time calculated for the SiC/C preform
241 should be closer to the real infiltration times since the chemical reaction should not delay infiltration
242 as much as in the C_f/C preform.
243 Figure 5 shows the evolution of bulk density of the infiltrated specimens with different dwell times
244 in the furnace at 1450 °C for both kinds of preforms under Ar flow (black dots) and under a vacuum
245 atmosphere (white dots). The red and blue lines are guides to the eye.
246 In general, lower densities are obtained when infiltrating under Ar flow, most likely because of gas
247 entrapment within the pores of the preform. Because of the set up used for infiltration, the surface of
248 the preform can be rapidly covered with Si after it melts preventing gas inside the pores from exiting
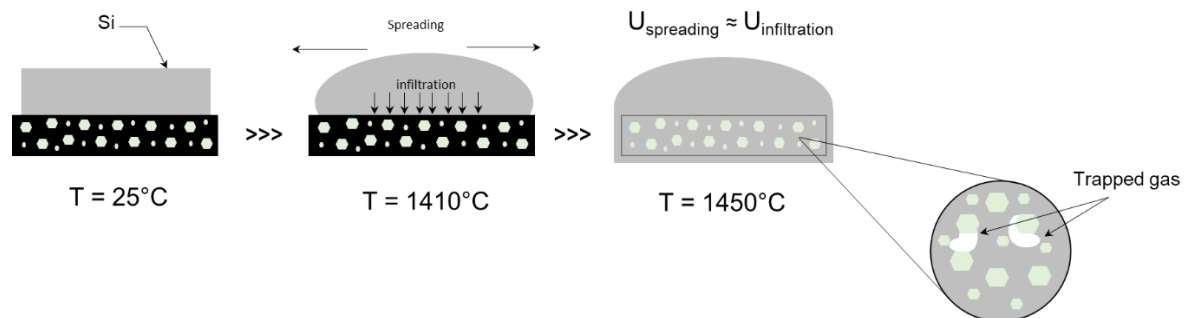249 the preform (see Figure 6).

250
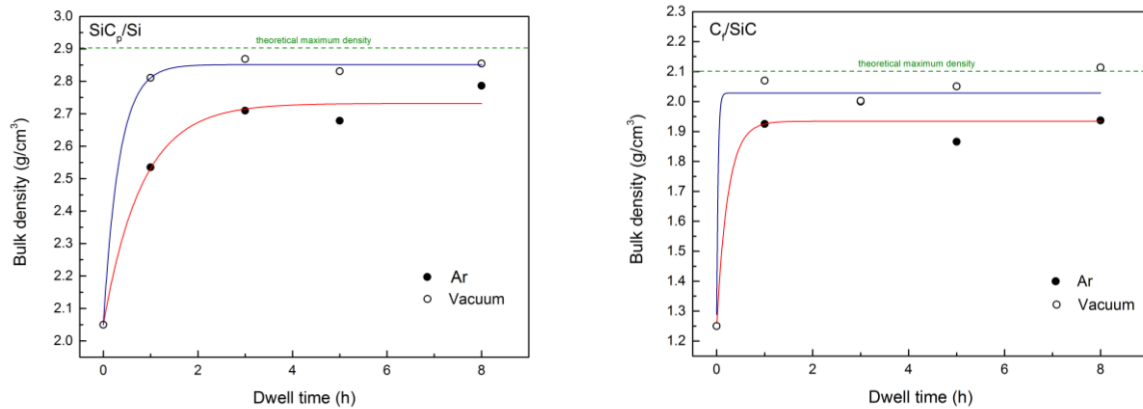
251
252 **Figure 5.** Bulk density as a function of dwell time at 1450 °C under Ar and vacuum atmospheres of
253 SiC$_P$/C preforms and C$_f$/C preforms.
254

255 The fact that longer dwell times yield denser materials provides more evidence of this phenomenon,
256 as gas bubbles can diffuse through the melt and out of the preform if given sufficient time. Further
257 proof of gas bubbles entrapment is provided by the evolution of bulk density with dwell time
258 obtained for infiltrations performed under vacuum. Not only higher values of bulk density are
259 obtained, but also a value of density close to the theoretical maximum density is obtained after 1 h at
260 1450 °C. The huge difference in density between the sample infiltrated for 1 h in Ar and under vacuum
261 can only be explained because of gas remaining within the microstructure for the sample infiltrated
262 in Ar, as models suggest that full vertical infiltration should occur in the first minutes.
263

264
265 **Figure 6.** Schematic representation of the infiltration process in SiC/C preforms under Ar flow.
266

267 The difference between densities achieved under Ar or vacuum is smaller for the C$_f$/SiC composite
268 than for SiC/C (see Figure 5). Because pores are wider for the C$_f$/C preform, and spreading of liquid
269 Si and thus infiltration proceeds slower because they are limited by the chemical reaction at the
270 infiltration front, gas can escape the pores easier as they are filled. Nevertheless, the slightly higher
271 densities obtained with vacuum suggest that gas can remain trapped within the smallest pores of the
272 preform during infiltration.
273

274 3.3 Microstructure of the composites.

275

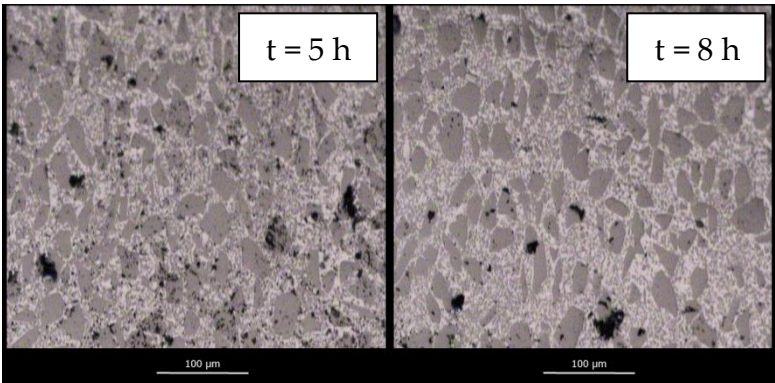276   - SiC$_P$/Si Composite Materials

277

278   Figure 7 shows a representative optical micrograph of a polished cross-section of a fully infiltrated

279   SiC$_P$/Si composite material at two different magnifications. The porous carbon matrix of the SiC$_P$/C

280   preform has been replaced with a dense Si matrix, and the bimodal SiC particle distribution is clearly

281   observed.

282   Figure 8 shows the evolution of microstructure at different dwell times for samples infiltrated under

283   Ar flow. Full vertical infiltration has been achieved for all samples. However, samples show large

284   residual open porosity, especially sample infiltrated with a dwell time of 1 h. The microstructures

285   support the idea that the lower values of density obtained under Ar flow are a consequence of gas

286   entrapment within the microstructure of the material. Consequently, even if full infiltration is

287   observed, large pores remain within the composite. This porosity decreases with increasing dwell

288   time as bubbles diffuse out of the preform.


289
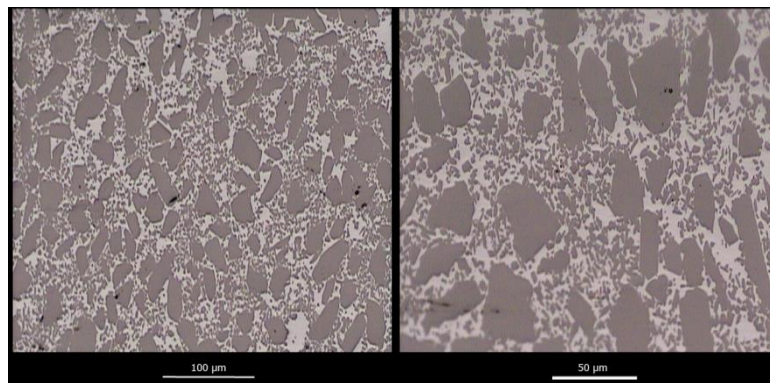
290   **Figure 7.** Representative optic micrographs of a fully infiltrated SiC$_P$/Si composite material.

291

292

293
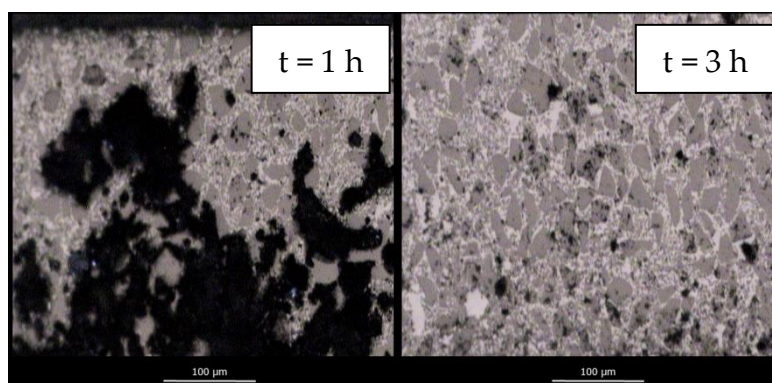
**Figure 8.** Evolution of the microstructure of SiC$_P$/Si composite materials infiltrated at 1450 ℃ in Ar flow atmosphere with different dwell time.

296

Further evidence of this phenomenon is given in Figure 9, where the evolution of the microstructure of SiC$_P$/Si composite materials infiltrated under vacuum is shown. No differences in the microstructure with dwell time are observed for samples infiltrated under vacuum. Furthermore, the absence of the large pores observed for samples infiltrated under Ar confirms that gas entrapment is responsible for the lower densities of those samples.

302

304
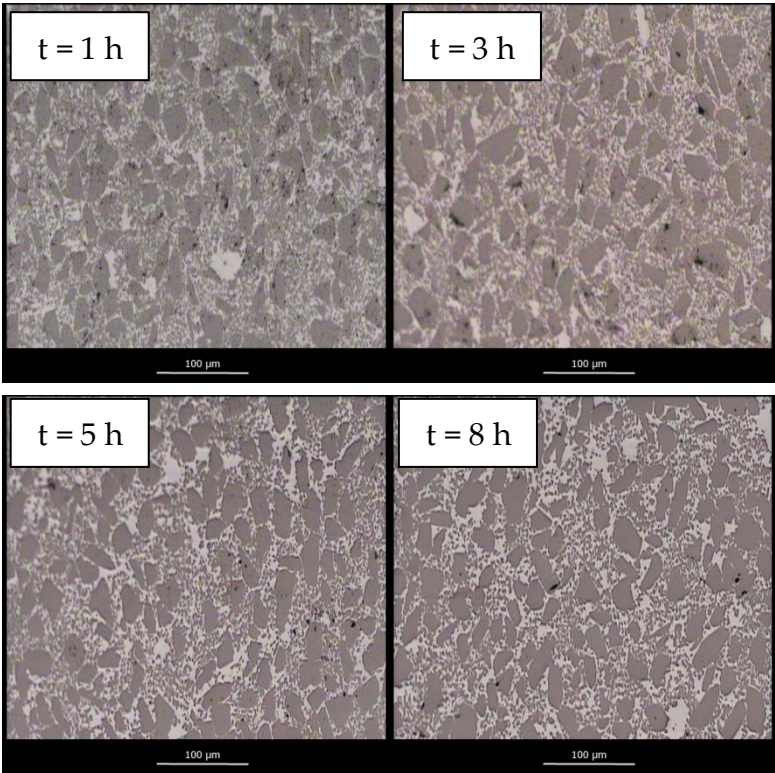
Figure 9. Evolution of the microstructure of SiC$_P$/Si composite materials infiltrated at 1450 ℃ under vacuum atmosphere with different dwell time.

307

Quantitative XRD analysis yielded β-SiC/α-SiC molar ratios between 0.05-0.2, which is consistent with the initial amount of C having fully reacted. The rather high dispersion in the beta/alfa molar

310   ratios measured can be mainly attributed to some heterogeneity in the C binder distribution within

311   the preform, as well to the dispersion in the A_{111}/A_{100} of the standards used to prepare the calibration

312   curve. The generated calibration curve for X ray quantitative analysis is shown in Figure 10.

313

314
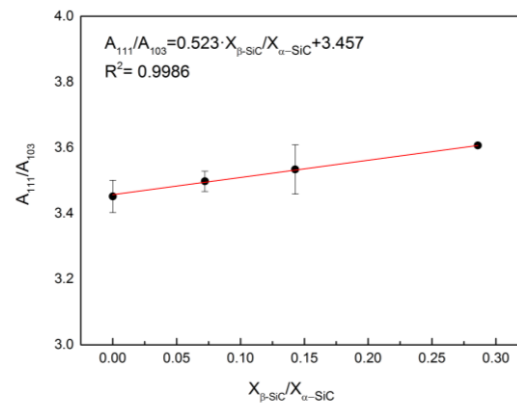
315   **Figure 10.** Calibration curve obtained from evaluating the relationship between the area below the

316   111 and the 103 diffraction peaks and the molar ratio between β-SiC and α-SiC.

317

318   - C_f/SiC Composite materials

319

320   Figure 16 shows two representative micrographs obtained with optical microscopy of polished cross-

321   sections of C_f/SiC fully infiltrated specimens at different magnification. 4 different phases are

322   observed within the microstructure, namely, unreacted amorphous carbon (continues dark brown

323   phase), carbon fibers (dark brown, circle or ellipse cross-section), unreacted silicon (white), and β-SiC

324   (light brown, faceted crystals). Residual porosity is depicted in black. The microstructure of the

325   preform is mimicked after infiltration but amorphous carbon has been partially dissolved and is now

326   covered in a continues layer of SiC. Silicon remains trapped within the residual porosity and carbon

327   fibers remain unaltered, with some minor amounts of fibers having been dissolved.

328

329
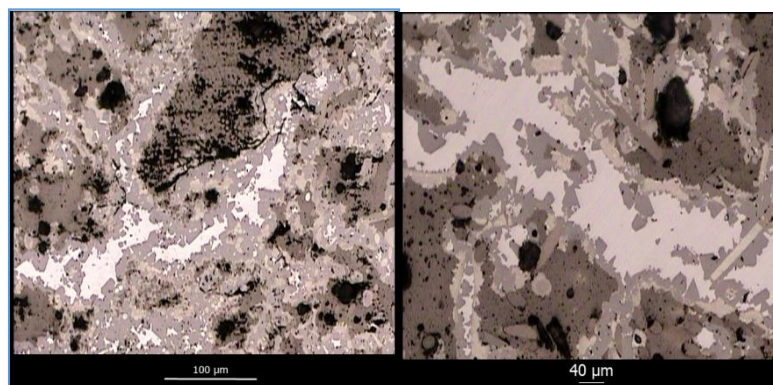
330   **Figure 11.** Representative micrographs of polished cross-sectioned C_f/SiC specimens.

331

332   As discussed in the previous section, because Si does not wet carbon or carbon fibers, infiltration in

333   this preform should be limited by the chemical reaction at the infiltration front, and should occur

334   therefore much slower than predicted by Darcy's law. Furthermore, because of the large content in

335   amorphous reactive carbon, pore reduction should play a major role in infiltration kinetics. Figure 12

336   shows evidence of severe pore reduction in C_f/SiC samples where even pore closure is observed for

337   smaller channels.

338

339
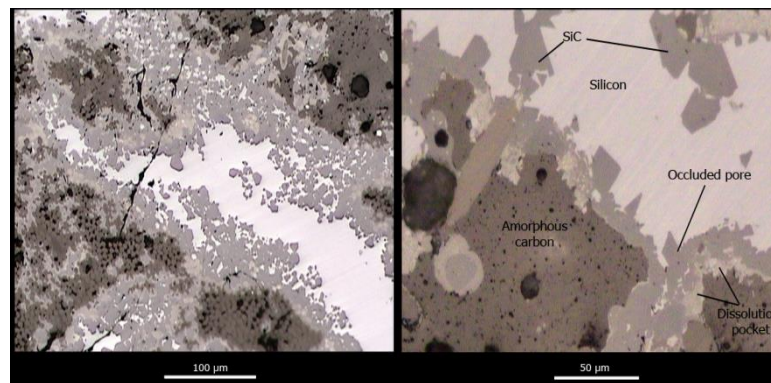
340   **Figure 12.** Pore reduction and pore closure phenomena in C_f/SiC composite materials during reactive

341   infiltration.

342

343   There were no large differences observed in the microstructure between samples infiltrated in Ar and

344   under vacuum, besides some additional residual porosity. After the SiC layer has covered the

345   amorphous carbon and the carbon fibers, its growth is controlled by diffusion of C and Si through

346   the SiC interface, and the growth kinetics become much slower so no large differences are observed

347   within the dwell times tested. There was some increase in carbon fiber dissolution with dwell time,

348   though, as shown in Figure 13, especially relevant for samples infiltrated with a dwell time of 5 and

349   8 h. This phenomenon could affect mechanical properties of the material negatively.

350   Figure 14 shows the interface formed between the carbon fiber bundles and the SiC and amorphous

351   carbon phases. An intimate contact between fibers and the amorphous carbon phase is observed.

352   However, this interface is rather weak and does not provide enough mechanical resistance. The

353   contact between the fibers and the SiC phase is defective and is achieved through an interface that

354   comprises dissolution pockets formed during early stages of infiltration and the nano-SiC that

355   precipitates upon cooling of the C-supersaturated Si within the dissolution pockets [14]

356

357

358
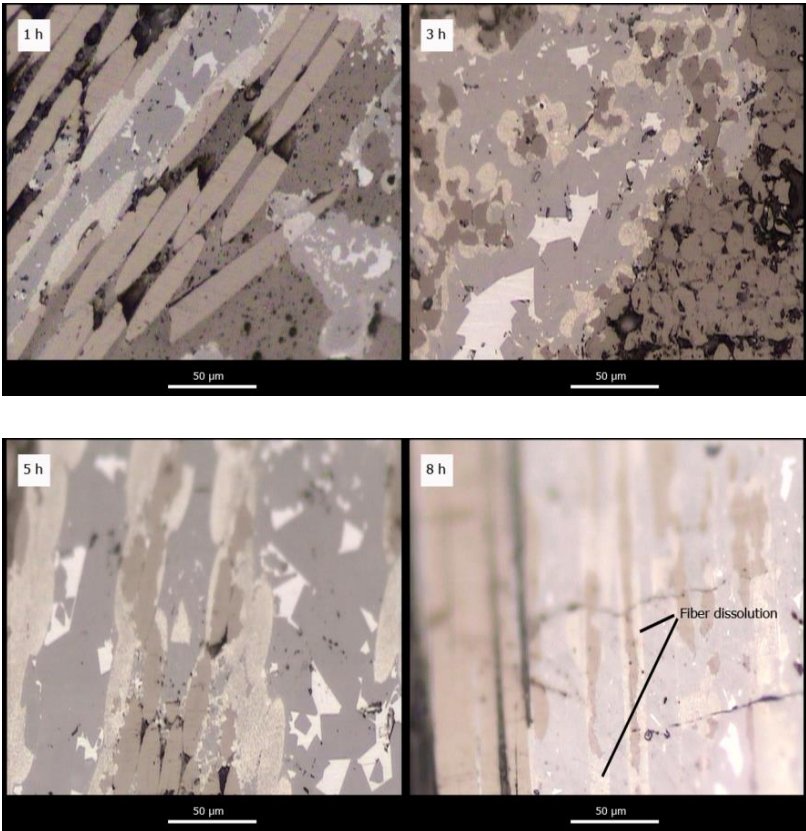
359   **Figure 13.** Evolution of carbon fibers during infiltration at different dwell times.

360

361

362

363   **Figure 14.** C_f/SiC and C_f/C interfaces in C_f/SiC composite materials.

364
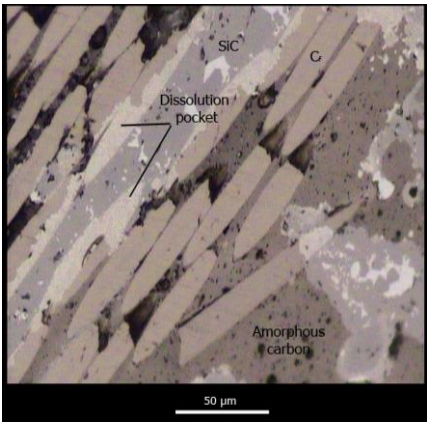
365   Table 4 shows the calculated composition after the selective etching. As expected no differences in

366   the amount of SiC phase are observed, yielding contents in SiC between 35-38% independently of the

367   dwell time. The small differences are attributed to the heterogeneous distribution of the phases in the

368   preform.

369

370   **Table 4.** Phase quantification of infiltrated C_f/SiC composite materials.

Atmosphere	Dwell time at 1450 ºC (h)	% SiC	% Si	% C_f+ C
Ar	1	37.6	5.3	57.1
	3	38.9	2.5	58.6
	5	38.8	7.0	54.1
	8	36.7	3.6	59.8
Vacuum	1	31.2	8.7	60.2
	3	30.0	7.7	62.7
	5	35.7	1.9	61.5
	8	35.0	3.5	62.7

371

372   3.4 Mechanical properties of composites Materials

373

374   After studying the effects of dwell time and atmosphere on infiltration and microstructure of the

375   materials, the optimum conditions were selected for each preform based on the quality of the material

376   and the shortest processing time. Mechanical properties of the produced composites under optimum

377   infiltration conditions were tested selecting the testing methods according to the potential

378   applications of each composite material. The optimum infiltration conditions for the SiC_P/C preforms

379   were selected as 1450 °C, with a dwell time of 1 h under vacuum atmosphere. The optimum

380   infiltration conditions for C_f/C preforms were selected as 1450 °C, with a dwell time of 1 h under

381   vacuum atmosphere.

382

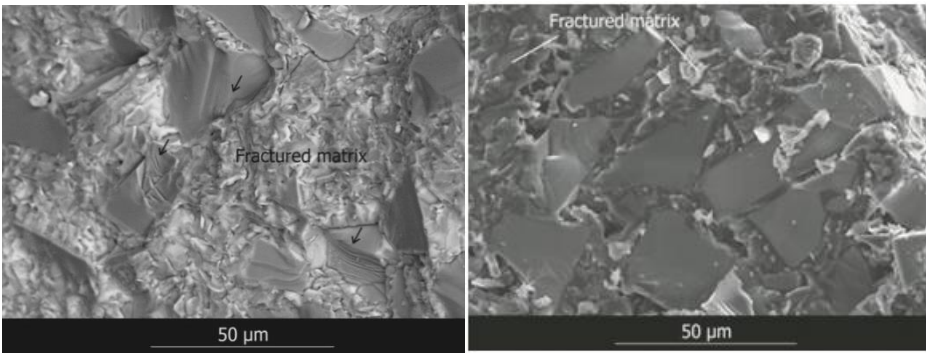383   - Mechanical properties of SiC_P/Si composite Material

384

385   Table 4 summarizes the measured mechanical properties for the SiC_P/Si composite material.

386   Mechanical performance of the material was characterized using the 3 point bending test and the

387   quasi-static compression test. As expected for a ceramic material, the SiC_P/Si composite exhibits

388   higher compressive resistance than flexural where the fracture is dominated by matrix cracking on

389   the tensile face. The material exhibits a high specific strength (bending strength divided by density)

390   compared to some metals and metal alloys [25,26].

391

392   **Table 4.** Measured mechanical properties for the SiC_P/Si composite material.

Material	Bending strength (MPa)	Compressive resistance (MPa)	Elastic Modulus (GPa)	Density (g/cm³)
SiC_P/Si	310	520	110	2.8

393

394   Figure 15 shows SEM images of the fracture surfaces of the material after mechanical testing, where

395   it is possible to observe that the main fracture mechanism of the material subjected to flexural stresses

396   is a mixture of interparticle/intraparticle mechanism, as most SiC particles appear broken (indicated
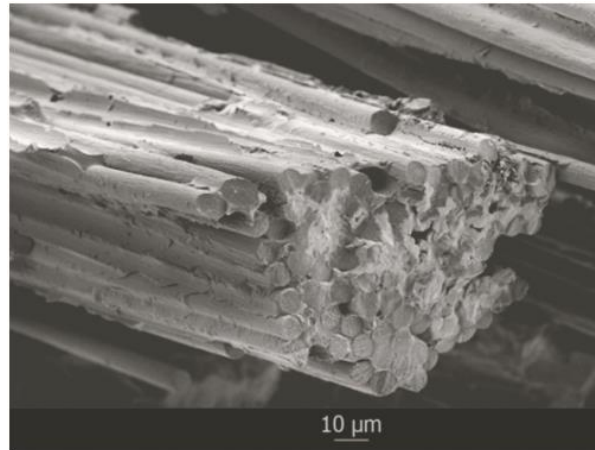
Figure 16. Fracture surface of the C_f/SiC composite material after the 3 point bending test.

5. Conclusions

Different porous carbon-containing preforms have been studied and characterized as candidates to be use in the synthesis of SiC-based composite materials by reactive infiltration. The infiltration process was successfully achieved and C_f/SiC and SiC_P/Si composite materials were obtained. The variables of atmosphere and dwell time were optimized for each preform, selecting a dwell time of 1 hour and vacuum atmosphere as the optimum conditions for infiltration of both preforms at 1450 °C. The most relevant mechanical properties for the applications of the different composite materials were measured. The C_f/SiC material shows outstanding properties to be used in ground and air transportation braking systems and could be used potentially in future reusable space transportation. The SiC_P/Si material shows excellent properties to be used in protection systems such as armored jackets or armored vehicles. Because of its thermal properties it could be implemented as shields in space vehicles to protect against minor impacts.

.

Conflicts of Interest: The authors declare no conflict of interest

References

1. E. Medvedovski, Ballistic performance of armor ceramics: Influence of design and structure. Part 1, Ceram. Int. 36 (2010) 2103–2115.
2. E. Medvedovski, Ballistic performance of armor ceramics: Influence of design and structure. Part 2, Ceram. Int. 36 (2010) 2117–2127.
3. P.G. Karandikar, G. Evans, S. Wong, M.K. Aghajanian, M. Sennett, A review of ceramics for armor applications, Advances in Ceramic Armor IV Ceramic and Engineering Science Proceedings, 29 (2009) 163-75.
4. R. Klement, S. Rolc, R. Mikulikova, J. Krestan, Transparent armor materials, J. Eur. Ceram. Soc. 28 (2008) 1091–1095.
5. H. Hald, Operational limits for reusable space transportation systems due to physical boundaries of C/SiC materials, Aerospace Sci. Tech. 7 (2003) 551–559.

457   6.   N.R. Calderón, M. Martínez-Escandell, J. Narciso, F. Rodríguez-Reinoso, J. Eur. Ceram. Soc. 29
458   (2009**)** 465.
459   7.   P. Greil, Near net shape manufacturing of ceramics, Mater. Chem. Phys. 61 (1999) 64-68
460   8.   A.R. de Arellano-Lopez, J. J. Martinez-Fernandez, P. Gonzalez, C. Dominguez, V. Fernandez-
461   Quero, M. Singh, Biomorphic SiC: A new engineering ceramic material, Appl. Ceram. Tech. 1
462   (2004) 56-57.
463   9.   N.R. Calderón, M. Martínez-Escandell, J. Narciso, F. Rodríguez-Reinoso. J. Amer. Ceram. Soc.
464   93 (2010) 1003.
465   10. R.P. Messner, Y.M. Chiang, Liquid-phase reaction-bonding of silicon carbide using alloyed
466   silicon-molybdenum melts, J. Am. Ceram. Soc., 73 (1990) 1193-1200.
467   11. Arpón, R.; Narciso, J.; Rodríguez-Reinoso, F.; M. Komatsu, M. Synthesis of mixed disilicides/SiC
468   composites by displacement reaction between metal carbides and silicon, Mater. Sci. Eng. A 380
469   (2004) 62–66.
470   12. Y. Wang, S. Tan, D. Jiang, The fabrication of reaction-formed silicon carbide with controlled
471   microstructure by infiltrating a pure carbon preform with molten Si, Ceram. Int. 30 (2004) 435-
472   439.
473   13. http://www.helm-project.eu/
474   14. M. Caccia, S. Amore, D. Giuranno, R. Novakovic, E. Ricci, J. Narciso. Towards optimization of
475   SiC/CoSi2 composite material manufacture via reactive infiltration: Wetting study of Si–Co
476   alloys on carbon materials, Journal of the European Ceramic Society 35 (2015), 4099-4106.
477   15. O. Coloma Esteban, M. Caccia, A. Camarano, J. Narciso. Composite manufacture of SiC/ZrSi$_2$
478   materials: assessing thermal compatibility between matrix and reinforcement, Advances in High
479   Temperature Ceramic Matrix Composites and Materials for Sustainable Development, 263
480   (2017) 75-84.
481   16. A. Camarano, M. Caccia, J. Narciso. Effect of Vacuum on Microstructure and Mechanical
482   Properties of Silicon Carbide Produced by Reactive Infiltration, Advances in High Temperature
483   Ceramic Matrix Compo sites and Materials for Sustainable Development; Ceramic Transactions,
484   Volume CCLXIII, 263 (2017) 323-331.
485   17. C. Garcia-Cordovilla, E. Louis, J. Narciso. Pressure infiltration of packed ceramic particulates by
486   liquid metals, Acta Mater., 47 (1999) 4461-4479. DOI: 10.1016/ S1359-6454(99)00318-3
487   18. A. Alonso, A. Pamies, J. Narciso, C. Garcia-Cordovilla, E. Louis, Evaluation of the wettability of
488   liquid aluminum with ceramic particulates (SiC, TiC, AI2O3) by means of pressure infiltration.
489   Metall. Trans. A, 24 (1993)1423-1432. DOI: 10.1007/BF02668210
490   19. M. Caccia, A. Camarano, D. Sergi, A. Ortona, J. Narciso, Wetting and Navier-Stokes Equation-
491   The Manufacture of Composites Materials, The Manufacture of Composite Materials, Wetting
492   and Wettability, Mahmood Aliofkhazraei, IntechOpen. DOI: 10.5772/61167.
493   20. S. Amore, D. Giuranno, R. Novakovic, E. Ricci, R. Nowak, N. Sobczak. Thermodynamic and
494   surface properties of liquid Ge–Si alloys, Calphad, 44 (2014) 95-101. DOI:10.1016/
495   j.calphad.2013.07.014
496   21. R. Novakovic, E. Ricci, F. Gnecco, D. Giuranno, G. Borzone, Surface and transport properties of
497   Au–Sn liquid alloys. Surf Sci., 599 (2005) 230-247. DOI:10.1016/j.susc. 2005.10.009. 134
498   22. I. Egry, E. Ricci, R. Novakovic, S. Ozawa, Surface tension of liquid metals and alloys — recent
499   developments, Adv. Colloid. Interface Sci.. 159 (2010) 198-212. DOI:10.1016/j.cis. 2010.06.009
500   23. N. Eustathopoulos , M.G. Nicholas, B. Drevet Wettability at High Temperatures. In: Cahn RW
501   (ed.). Pergamon Materials Series. Cambridge: Pergamon; 1999. ISBN: 978-0-08-042146-9
502   24. Y. Yang, A. C. Aplin, Influence of lithology and compaction on the pore size distribution and
503   modeled permeability of some mudstones from the Norwegian margin, Mar. Pet. Geol. 15 (1998)
504   163-175.
505   25. J. Chen, B. Young, B. Uy, Behavior of High Strength Structural Steel at Elevated Temperatures,
506   J. Struct. Eng. 132 (2006) 1948-1954.
507   26. http://www.specialmetals.com/documents/Inconel%20alloy%20718.pdf   (last   consulted
508   12/06/2019).